Scavenging of soluble and immobilized CCL21 by ACKR4 regulates peripheral dendritic cell emigration

Cameron R. Bastow[a], Mark D. Bunting[a,b], Ervin E. Kara[a], Duncan R. McKenzie[a,1], Adriana Caon[a], Sapna Devi[c], Lynn Tolley[d], Scott N. Mueller[c], Ian H. Frazer[d], Natasha Harvey[e], Mark R. Condina[f], Clifford Young[f], Peter Hoffmann[f], Shaun R. McColl[a,2,3], and Iain Comerford[a,2,3]

[a]Chemokine Biology Laboratory, Department of Molecular and Biomedical Science, School of Biological Science, The University of Adelaide, Adelaide, SA 5005, Australia; [b]Genome Editing Laboratory, School of Medicine, The University of Adelaide, Adelaide, SA 5000, Australia; [c]Department of Microbiology and Immunology, The Peter Doherty Institute for Infection and Immunity, The University of Melbourne, Melbourne, VIC 3000, Australia; [d]The University of Queensland Diamantina Institute, Translational Research Institute, Woolloongabba, QLD 4102, Australia; [e]Centre for Cancer Biology, University of South Australia and SA Pathology, Adelaide, SA 5000, Australia; and [f]Future Industries Institute, University of South Australia, Mawson Lakes, SA 5095, Australia

Edited by Jason G. Cyster, University of California, San Francisco, CA, and approved March 16, 2021 (received for review January 11, 2021)

Leukocyte homing driven by the chemokine CCL21 is pivotal for adaptive immunity because it controls dendritic cell (DC) and T cell migration through CCR7. ACKR4 scavenges CCL21 and has been shown to play an essential role in DC trafficking at the steady state and during immune responses to tumors and cutaneous inflammation. However, the mechanism by which ACKR4 regulates peripheral DC migration is unknown, and the extent to which it regulates CCL21 in steady-state skin and lymph nodes (LNs) is contested. Specifically, our previous findings that CCL21 levels are increased in LNs of ACKR4-deficient mice [I. Comerford et al., *Blood* 116, 4130–4140 (2010)] were refuted [M. H. Ulvmar et al., *Nat. Immunol.* 15, 623–630 (2014)], and no differences in CCL21 levels in steady-state skin of ACKR4-deficient mice were reported despite compromised CCR7-dependent DC egress in these animals [S. A. Bryce et al., *J. Immunol.* 196, 3341–3353 (2016)]. Here, we resolve these issues and reveal that two forms of CCL21, full-length immobilized and cleaved soluble CCL21, exist in steady-state barrier tissues, and both are regulated by ACKR4. Without ACKR4, extracellular CCL21 gradients in barrier sites are saturated and nonfunctional, DCs cannot home directly to lymphatic vessels, and excess soluble CCL21 from peripheral tissues pollutes downstream LNs. The results identify the mechanism by which ACKR4 controls DC migration in barrier tissues and reveal a complex mode of CCL21 regulation in vivo, which enhances understanding of functional chemokine gradient formation.

chemokines | atypical chemokine receptors | migration | dendritic cells

CCL21 is a chemokine that mediates recruitment of multiple leukocyte subsets through CCR7-mediated signaling during the steady state and inflammation. CCL21 plays crucial roles in priming adaptive immunity via governing egress of dendritic cells (DCs) from barrier tissues and T cell entry and positioning in secondary lymphoid organs (1–5). A well-characterized site of CCL21 gradient formation is the skin, where CCL21 is secreted by lymphatic endothelial cells (LECs) and immobilized on extracellular heparan sulfate moieties via interactions with the charged, elongated C-terminal tail of CCL21 (6–8). Here, immobilized CCL21 gradients are essential for interstitial DC trafficking toward lymphatic vessels (LVs) (8), after which CCL21 further contributes to LV attachment (9), infiltration (10), downstream luminal migration (11), and migration from the lymph node (LN) subcapsular sinus (SCS) to the paracortex (12). In-vitro studies have shown that the C-terminal tail of CCL21 can also be proteolytically cleaved by mature DCs to generate solubilized CCL21 (13), with signaling properties distinct from another soluble CCR7 ligand, CCL19 (14, 15). While CCL19 is dispensable for steady-state DC migration (16), important questions regarding the in vivo processing and function of cleaved CCL21 remain.

Both forms of CCL21 are also ligands for the atypical chemokine receptor ACKR4 (17), which regulates chemokine bioavailability rather than directly mediating cell migration. ACKR4 expression has been identified in multiple barrier tissues (18–20) and lymphoid tissues (12, 21) where expression is largely restricted to stromal cell populations, with the exception of germinal-center B cells (22). Despite clear evidence of ACKR4 scavenging of CCL21 in vitro, the extent to which it regulates CCL21 in vivo is disputed. We have shown increased CCL21 in the LNs of *Ackr4*$^{-/-}$ mice, which was associated with exacerbated Th17 responses in autoimmunity (23) and an ACKR4-dependent increase in CCL21 in tumors that promotes antitumor immunity (24). However, no differences in dermal CCL21 abundance were previously reported in steady-state *Ackr4*$^{-/-}$ mice despite steady-state CCR7-dependent DC migratory defects being independent of CCL19 (19), and the contribution of ACKR4 in regulating LN CCL21 abundance has been disputed despite a clear role for ACKR4 in maintaining interfollicular CCL21 gradients in LN (12). These discrepancies have remained unresolved but point to previously unrecognized complexity in ACKR4-dependent regulation of CCL21 in both barrier and lymphoid tissues.

Significance

The immune system relies on coordinated interactions between motile cells guided by molecules known as chemokines. However, processes that control chemokine distribution in complex in vivo microenvironments are poorly understood. Dendritic cells in barrier tissues require the chemokine CCL21 to enter lymphatic vessels during tissue egress. Here, we demonstrate that ACKR4 shapes CCL21 distribution in barrier tissues and prevents leakage of CCL21 from the tissue. Without ACKR4, extracellular CCL21 gradients in barrier sites are saturated and nonfunctional, DCs cannot home directly to lymphatic vessels, and excess soluble CCL21 from peripheral tissues pollutes lymph nodes. The results increase understanding of regulation of dendritic cell egress and chemokine distribution in vivo and raise new questions regarding the function of solubilized CCL21.

Author contributions: C.R.B., S.D., S.N.M., P.H., S.R.M., and I.C. designed research; C.R.B., M.D.B., E.E.K., D.R.M., A.C., S.D., L.T., S.N.M., M.R.C., C.Y., and I.C. performed research; S.N.M., I.H.F., N.H., and P.H. contributed new reagents/analytic tools; C.R.B., S.D., M.R.C., C.Y., P.H., and I.C. analyzed data; and C.R.B., S.R.M., and I.C. wrote the paper.

The authors declare no competing interest.

This article is a PNAS Direct Submission.

[1]Present address: Immunosurveillance Laboratory, Francis Crick Institute, London NW1 1AT, United Kingdom.

[2]S.R.M. and I.C. contributed equally to this work.

[3]To whom correspondence may be addressed. Email: shaun.mccoll@adelaide.edu.au or iain.comerford@adelaide.edu.au.

This article contains supporting information online at https://www.pnas.org/lookup/suppl/doi:10.1073/pnas.2025763118/-/DCSupplemental.

Published April 19, 2021.

Results and Discussion

ACKR4 Regulates Soluble CCL21 in Barrier Tissues. While investigating the contribution of ACKR4 in regulating chemokine bioavailability at barrier sites, we detected hyperabundant CCL21 in all ACKR4-deficient barrier tissues examined at levels 2- to 10-fold greater than wild type (WT) (Fig. 1*A*). No difference in ACKR4 ligands CCL19 and CCL25 was detected in these tissues, with the exception of the skin where CCL19 was ~twofold greater in *Ackr4*$^{-/-}$ mice compared to WT mice (Fig. 1*A*). Hyperabundant CCL21 in skin observed here was in contrast to a published report (19) and highlighted another instance of a disparity between laboratories regarding CCL21 quantitation in *Ackr4*$^{-/-}$ mice (12, 19, 21, 23, 25). Because these studies differed in the capture antibody utilized for CCL21 quantification via enzyme-linked immunosorbent assay (ELISA), we compared the ability of these antibodies to bind both forms of murine CCL21. Cleaved CCL21 (8kDa) was generated from recombinant full-length CCL21 (12kDa) as previously described (13), and both CCL21 forms were subsequently assayed by Western blot using the various ELISA CCL21 capture antibodies used in previous studies. Both full-length and cleaved isoforms of CCL21 were detected with polyclonal goat anti-CCL21 (R&D Systems AF457) used in Fig. 1*A* and in our previous publications (23–25) (Fig. 1*B*). However, the monoclonal rat anti-CCL21 antibody (R&D Systems MAB457), the capture component of the murine CCL21 ELISA DuoSet kit widely utilized (12, 19, 21), only detected full-length CCL21 (Fig. 1*B*). Reblotting the membrane with a third anti-CCL21 (Peprotech 500-P114) previously used by others (13) confirmed that cleaved CCL21 remained present but was not detected by MAB457 (Fig. 1*B*). ELISA analysis of the tissue samples in Fig. 1*A* using MAB457 anti-CCL21 as the capture antibody reproduced the results reported by Bryce et al. (19), with no difference in skin CCL21 between WT and ACKR4-deficient mice (Fig. 1*C*). This was also apparent in the lungs of *Ackr4*$^{-/-}$ mice (Fig. 1*C*); however, statistically significant differences in full-length CCL21 abundance were detected in the small intestine and vagina (Fig. 1*C*). We also reanalyzed serum samples from WT and *Ackr4*$^{-/-}$ mice and show that the hyperabundant CCL21 in *Ackr4*$^{-/-}$ blood we previously reported (23) is entirely composed of cleaved CCL21 (*SI Appendix*, Fig. S1). In light of the finding that MAB457 does not detect cleaved CCL21, this forces a reinterpretation of the data reported by Bryce et al. and others who have used this reagent to quantify CCL21 in vivo (12, 19, 21). Thus, our data reveal that CCL21 cleavage occurs in barrier tissues during the steady state in vivo and that ACKR4 is crucial in limiting accumulation of solubilized CCL21. At all barrier sites examined, the magnitude of cleaved CCL21 hyperabundance in *Ackr4*$^{-/-}$ mice strongly correlated with the level of *Ackr4* messenger RNA (mRNA) detected in WT barrier tissue (Fig. 1*D*), linking the extent of CCL21 regulation in tissues to the local expression level of ACKR4. As anticipated, chemokine regulation via ACKR4 operated post-transcriptionally, as mRNAs for all ACKR4 ligands were present at similar levels in WT and *Ackr4*$^{-/-}$ tissues (Fig. 1*E*). CCL21 hyperabundance in *Ackr4*$^{-/-}$ ear skin was not due to any increase in the number of LECs, the predominant cellular source of CCL21 (6–8) (Fig. 1*F*). Additionally, potential "passenger DNA" from 129SV embryonic stem cells identified flanking the mutated *Ackr4* locus (26) did not account for increased CCL21 levels in *Ackr4*$^{-/-}$ mice as there was no difference in skin CCL21 abundance between C57BL/6J and 129SV mice (*SI Appendix*, Fig. S1*B*). Together, these data unequivocally demonstrate a key role for ACKR4 in scavenging soluble CCL21 in barrier tissues.

ACKR4 Shapes Extracellular Gradients of CCL21 in Barrier Tissues. To investigate whether ACKR4 also regulates full-length CCL21, gradients of immobilized CCL21 were visualized in situ, as the tissue leach-out assays used for ELISA analyses likely bias toward detection of soluble CCL21. Of note, detection of extracellular CCL21 in skin utilized the AF457 anti-CCL21 antibody. Thus, while both CCL21 forms are detected with this reagent via ELISA, conceptually it is unlikely that significant quantities of soluble chemokine would remain in tissue samples given the extensive washing steps involved. Consistent with previous findings (8), CCL21 staining in WT skin was most intense proximal to LYVE-1^{+} LVs, and the interstitial areas between LVs and CD31^{+} vasculature were largely devoid of CCL21 (Fig. 2 *A* and *B*). Conversely, in *Ackr4*$^{-/-}$ skin, hyperabundant CCL21 was present throughout the interstitial spaces and also littered LVs and CD31^{+} vasculature (Fig. 2 *A* and *B*). Quantitation of CCL21 intensity in WT images revealed that CCL21 intensity was greatest at the LV edge and was significantly decreased in areas distant from LVs (Fig. 2*C*). Surprisingly, we also detected a gradient of CCL21 most intense at the LV edge in *Ackr4*$^{-/-}$ dermis; however, the intensity of CCL21 was two- to threefold greater in *Ackr4*$^{-/-}$ tissue compared to WT tissue at each distance measured from LVs (Fig. 2*C*). As anticipated, CCL21 intensity in WT skin did not significantly change relative to the distance from CD31^{+} vessels (Fig. 2*D*), consistent with the role for CCL21 in LV homing. Again, CCL21 intensity was two- to threefold greater in *Ackr4*$^{-/-}$ tissue compared to WT tissue at all distances from CD31^{+} vessels (Fig. 2*D*). Therefore, unlike its role in the LN SCS (12), ACKR4 was not required to generate dermal CCL21 gradients but instead regulated the overall abundance of CCL21 within gradients.

Previous studies with *Ackr4*^{EGFP} mice identified cutaneous expression of ACKR4 in keratinocytes and minor populations of dermal LECs and hematopoietic cells (18, 19). To identify the cellular source of ACKR4 regulating dermal CCL21 during the steady state, we first generated bone marrow chimeras. Chimeric mice demonstrated that radio-resistant cells mediated the ACKR4-dependent regulation of both forms of CCL21, strongly implicating stromal cells in the regulation of dermal CCL21 (*SI Appendix*, Fig. S2 *A* and *B*). Surprisingly, greater *Ackr4* expression was measured in whole dermis compared to epidermis (*SI Appendix*, Fig. S2*C*). To reconcile this, we sorted all major stromal cell subsets from both the epidermis and dermis and Langerhans cells as they are radio resistant and persist in bone marrow chimeras as the same genotype as stromal cells (27) (*SI Appendix*, Fig. S2 *D* and *E*). Dermal fibroblasts displayed the greatest *Ackr4* expression in sorted cell populations, followed by interfollicular epidermal keratinocytes, and dermal double-negative cells (CD45^{-}CD31^{-}CD140α^{-}CD90^{-}), which includes smooth muscle cells and pericytes. Fibroblast expression of *Ackr4* identified here supports previous studies with human and mouse dermal fibroblasts (28, 29) and mirrors that observed in the small intestine where ACKR4 expression is restricted to submucosal fibroblasts (20). Together, these data support a model whereby ACKR4 expression by fibroblasts and other non-epithelial cells throughout the dermis regulate the overall abundance of CCL21 in interstitial spaces. Additionally, keratinocyte ACKR4 expression may assist in chemokine regulation given the prevalence of solubilized CCL21 in the skin during the steady state.

DC Mobilization to LVs Is Impaired in ACKR4-Deficient Skin. Steady-state recruitment of DCs into LNs from the skin is perturbed in *Ackr4*$^{-/-}$ mice (12, 18, 19); however, the mechanisms underlying this defect remain unknown. While a previous report implied no role for CCL21 in defective DC egress in *Ackr4*$^{-/-}$ mice (19), neither soluble CCL21 nor immobilized CCL21 gradients were measured in that study. Importantly, immobilized CCL21 gradients are configured within a narrow signal-to-noise range in vivo (30), hence ectopic or endogenous saturation of dermal CCL21 gradients disrupts DC egress (8, 31). We therefore hypothesized that aberrant CCL21 gradients and/or excess soluble CCL21 underpins perturbed DC egress in *Ackr4*$^{-/-}$ mice. To investigate CCL21 gradient functionality in *Ackr4*$^{-/-}$ tissue, activated bone marrow-derived DCs (BMDCs) were fluorescently labeled and incubated atop ear sheets from WT or *Ackr4*$^{-/-}$ mice. In this model, BMDCs enter the dermis and migrate toward LVs in a CCR7-dependent manner utilizing the

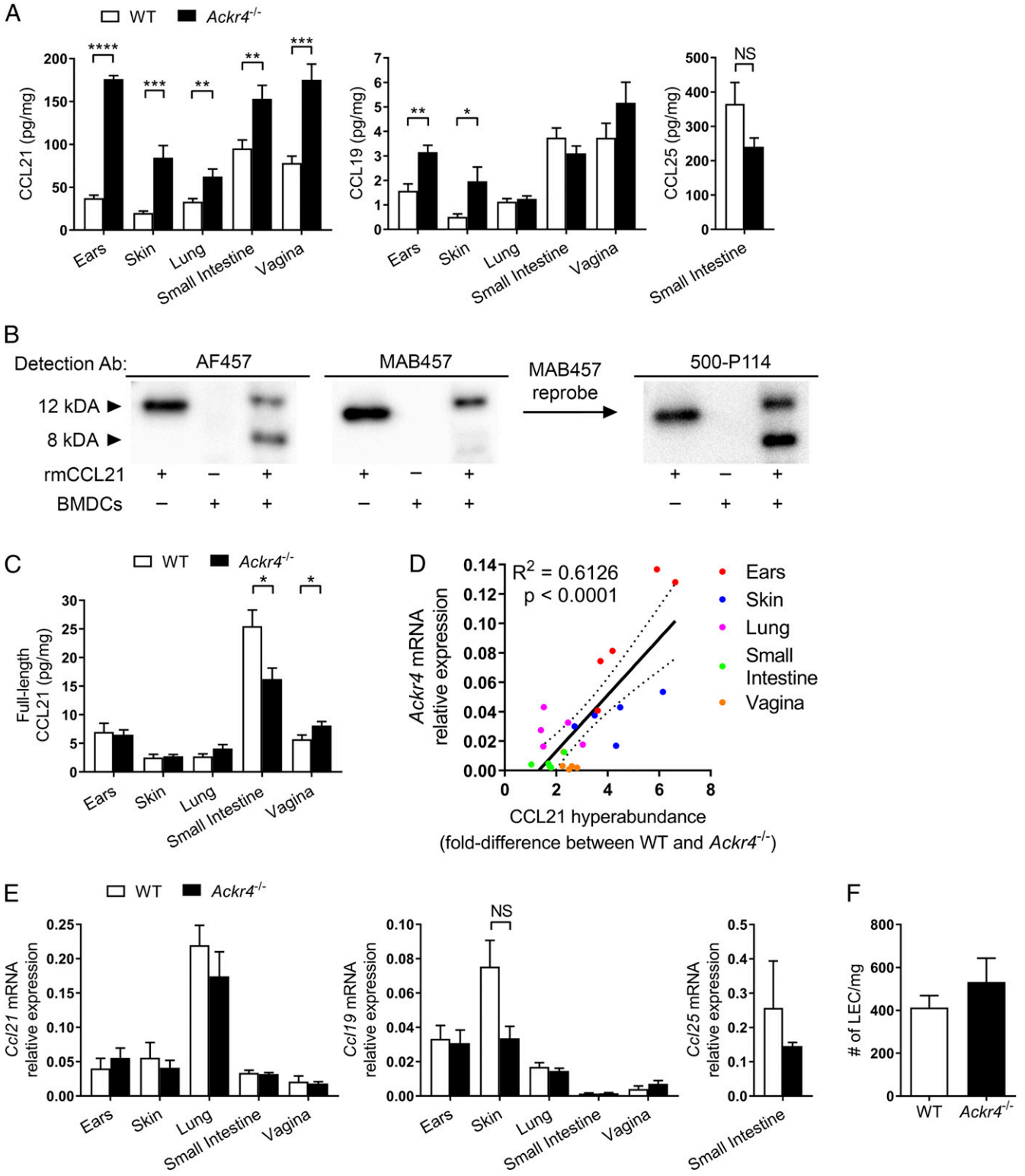

Fig. 1. ACKR4 regulates solubilized CCL21 in barrier tissues. (*A*) Quantity of total CCL21, CCL19, and CCL25 (picograms/milligram) leached out of resting barrier tissues from WT and *Ackr4*$^{-/-}$ mice, determined by ELISA. (*B*) Detection of full-length (12kDA) and BMDC-cleaved (8kDA) recombinant-mouse CCL21 with different commercial antibodies by Western blot. Membranes probed with the MAB457 antibody were subsequently reprobed with another commercial antibody. (*C*) Quantity of full-length CCL21 (pg/mg) leached out of resting barrier tissues from *A*, determined by ELISA. (*D*) Linear correlation between barrier-tissue *Ackr4* mRNA expression relative to *Rplp0*, and the fold difference of total CCL21 abundance between WT and *Ackr4*$^{-/-}$ mice. (*E*) Expression of *Ccl21*, *Ccl19*, and *Ccl25* mRNA relative to *Rplp0* in resting barrier tissues from WT and *Ackr4*$^{-/-}$ mice. (*F*) Number of LECs (CD45$^-$Ter119$^-$CD31$^+$gp38$^+$) per milligram of ear dermis in resting WT and *Ackr4*$^{-/-}$ mice. (*A*, *C*, and *F*) Data pooled from two independent experiments, $n = 5$ to 10 mice/strain ± SEM, two-tailed unpaired Student's *t* test, except *D*, linear regression with 95% CI (dotted lines). For graphs with multiple tissues, two-tailed unpaired Student's *t* test was performed between strains for a given tissue. (*B*) Data representative of two independent experiments. *$P < 0.05$, **$P < 0.01$, ***$P < 0.001$, and ****$P < 0.0001$.

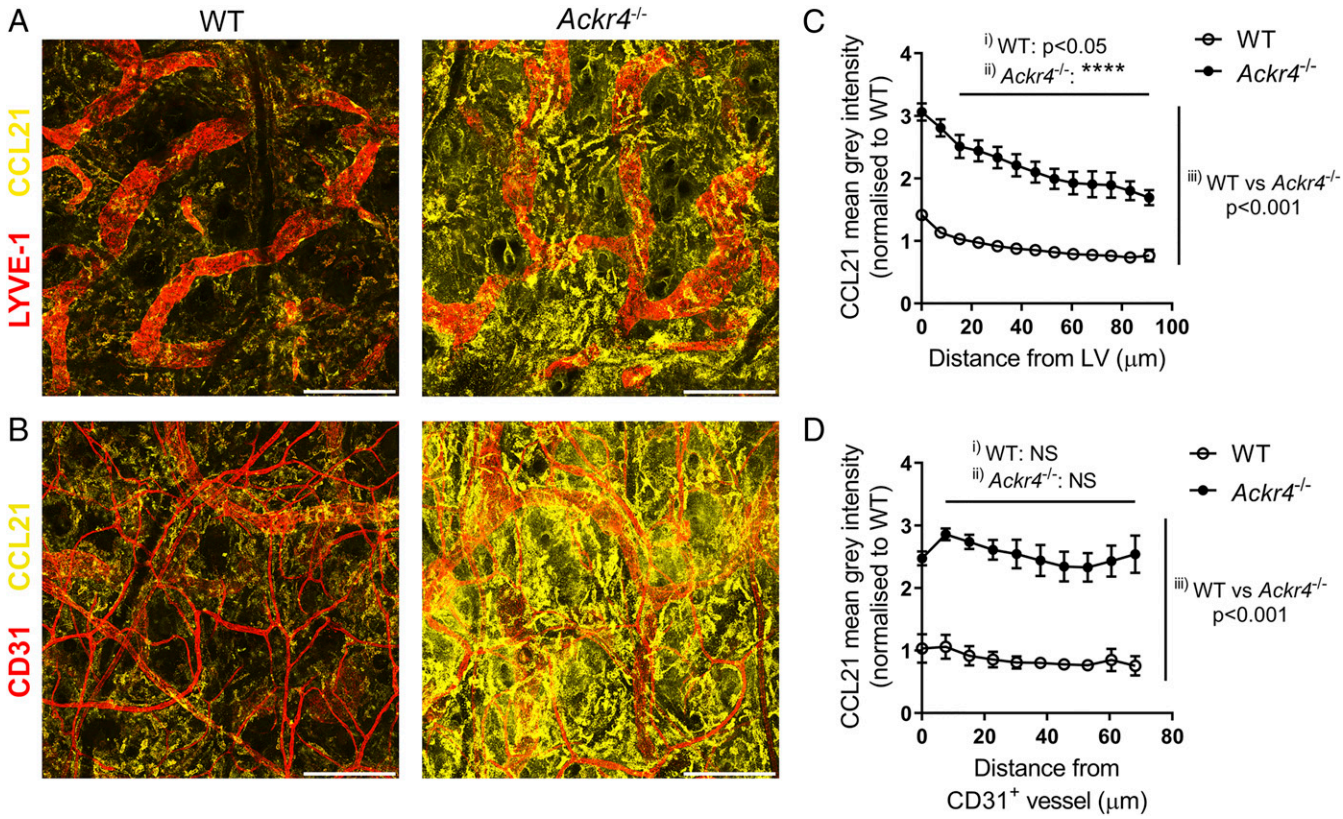

Fig. 2. ACKR4 regulates interstitial CCL21 gradients in the skin. (*A* and *B*) Z-stack projections of unfixed, nonpermeabilized whole-mount ear sheets from resting WT and *Ackr4*$^{-/-}$ mice, stained CCL21 (yellow) and LYVE-1 (red) (*A*) or CD31 (red) (*B*). (Scale bar, 200 μm.) (*C*) Quantitation of CCL21 mean gray intensity (normalized to average WT intensity) at defined distances from the nearest lymphatic vessel (0 μm) from images in *A*. (*D*) Quantitation of CCL21 mean gray intensity (normalized to average WT intensity) at defined distances from the nearest CD31^{+} vessel (0 μm) from images in *B*. (*A* and *C*) Images representative of and data pooled from two independent experiments, WT $n = 4$, *Ackr4*$^{-/-}$ $n = 5$. (*C*) Each dot represents the mean of biological replicates, within which technical replicates were averaged ± SEM. (*B* and *D*) Images and data from WT $n = 2$, *Ackr4*$^{-/-}$ $n = 3$. (*D*) Each dot represents the mean of biological replicates, within which technical replicates were averaged ± SEM. (*C* and *D*) Two-way ANOVA with Sidak's multiple comparison test for CCL21 intensity between a defined distance from the vessel and the vessel edge in *i*) WT tissue, *ii*) *Ackr4*$^{-/-}$ tissue, or *iii*) CCL21 intensity between WT and *Ackr4*$^{-/-}$ tissue at a defined interstitial distance. ****$P < 0.0001$.

endogenous immobilized CCL21 gradient (8). Within 45 min, most BMDCs had entered WT ear sheets and homed to LVs (Fig. 3*A*). Conversely, a large proportion of BMDCs in *Ackr4*$^{-/-}$ ear sheets remained within interstitial areas between LVs (Fig. 3*A*). Indeed, quantitation revealed significantly fewer BMDCs associated with LVs in ACKR4-deficient tissue (Fig. 3*B*). As previous studies found no role for CCL19 in steady-state DC egress from WT and *Ackr4*$^{-/-}$ skin (16, 19), the disrupted CCL21 distribution shown in our study now implicates dysregulated dermal CCL21 in aberrant DC egress from *Ackr4*$^{-/-}$ skin during the steady state.

To further interrogate the function of ACKR4 in DC egress in an intact in vivo setting, intravital microscopy was performed. BMDCs were injected subcutaneously into footpads of WT or *Ackr4*$^{-/-}$ hosts with LPS and fluorescently labeled anti–LYVE-1 antibody for visualization of LVs as previously described (9). After 12 to 21 h, blood capillaries were labeled by intravenous injection of Evans Blue dye, and BMDCs in close proximity to LVs were imaged. In WT hosts, BMDCs were visualized migrating toward, attaching to, and entering LVs (Fig. 3*C* and Movie S1). In contrast, numerous BMDCs close to LVs in *Ackr4*$^{-/-}$ hosts were visualized migrating away from, or perpendicular to, LVs (Fig. 3*C* and Movie S2). Interestingly, some BMDCs in *Ackr4*$^{-/-}$ hosts attached and crawled along blood capillaries despite close proximity to LVs (Fig. 3*C* and Movie S3), possibly responding to aberrant CCL21 at these surfaces in vivo (Fig. 2*B*). Plotting BMDC migratory tracks relative to LVs revealed that the majority of BMDCs tracked in WT hosts moved toward LVs, whereas BMDC migration in *Ackr4*$^{-/-}$ hosts was less uniform (Fig. 3*D*). BMDCs in WT hosts were significantly closer to LVs within 11 min of tracking, while there was no significant migration of BMDCs toward LVs in *Ackr4*$^{-/-}$ hosts during 20 min of tracking (Fig. 3*E*). Accordingly, BMDCs in WT hosts migrated closer to LVs than BMDCs in *Ackr4*$^{-/-}$ hosts within 10 min of tracking (Fig. 3*E*). There was no difference in the initial distance of tracked BMDCs from LVs between hosts (*SI Appendix*, Fig. S3*A*), thus defective BMDC migration was not due to cells being outside of the postulated range of haptotactic gradients (8). There was also no difference in average speed or track straightness between BMDCs in WT and *Ackr4*$^{-/-}$ hosts (*SI Appendix*, Fig. S3 *B* and *C*); however, these parameters in LPS-activated BMDC migration are largely independent of CCR7 (32). Rather, when CCR7-dependent migration toward LVs was measured, BMDCs in *Ackr4*$^{-/-}$ hosts displayed markedly reduced velocity (Fig. 3*F*) and homing efficiency (i.e., track straightness toward the nearest LV, Fig. 3*G*), compared to BMDCs in WT hosts. Together, these data show that inefficient LV homing underlies impaired DC egress in ACKR4-deficient skin.

Skin-Expressed ACKR4 Controls DC Egress to LN. To date, all studies investigating the effect of ACKR4 deletion on DC trafficking have been conducted in broad *Ackr4*$^{-/-}$ mice (12, 18, 19). Defects in steady-state DC trafficking have been attributed to dysregulated

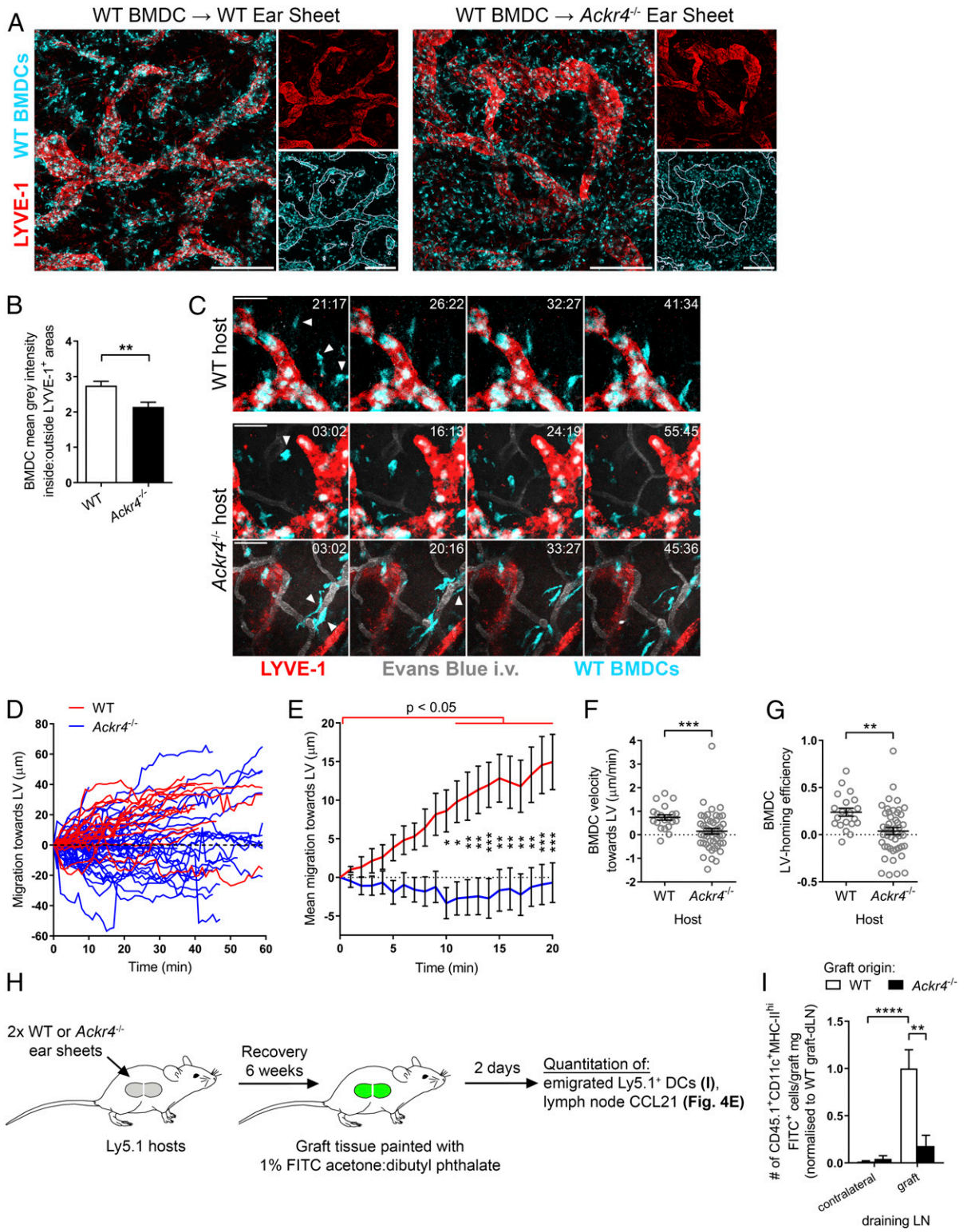

Fig. 3. ACKR4 regulation of dermal CCL21 is required for efficient DC LV homing and emigration. (*A*) Z stacks of WT and *Ackr4*$^{-/-}$ ears after BMDC crawl in. LYVE-1 (red), BMDCs (cyan), LV outline (white). (Scale bar, 200 μm.) (*B*) BMDCs inside:outside LV areas from *A*. (*C*) Z stacks and time stamps (minutes:seconds) of BMDCs in WT and *Ackr4*$^{-/-}$ hosts. Arrows highlight migrating BMDCs (cyan). (Scale bar, 50 μm.) (*D*) Displacement of BMDCs relative to nearest LV in WT and *Ackr4*$^{-/-}$ hosts. Lines represent one BMDC. (*E*) Mean displacement of BMDCs relative to nearest LV for first 20 min. Statistical comparisons in WT between 0 min and 11 to 20 min inclusive were $P < 0.05$, no significant differences across time points in *Ackr4*$^{-/-}$. Asterisks show comparisons between WT and *Ackr4*$^{-/-}$. (*F*) Velocity and (*G*) lymphatic-homing efficiency of BMDCs from *E*. (*H*) Schematic of experiment in *I* and Fig. 4*E*. (*I*) FITC^{+} host-derived DCs in graft-draining and contralateral LNs 48 h post-FITC painting. (*A* and *B*) Representative of two independent experiments, $n = 9$ mice/strain. (*B*) ± SEM, two-tailed unpaired Student's *t* test. (*C*–*G*) Images representative of two independent experiments, $n = 4$ mice/host strain total ± SEM, (*E*) two-way ANOVA with Sidak's multiple comparison test, and (*F* and *G*) two-tailed unpaired Student's *t* test. (*I*) Data from three independent experiments, $n = 14$ WT graft recipients, $n = 4$ *Ackr4*$^{-/-}$ graft recipients, ± SEM, two-way ANOVA with Sidak's multiple comparison test. *$P < 0.05$, **$P < 0.01$, ***$P < 0.001$, and ****$P < 0.0001$.

CCL21 gradients within the LN resulting from a loss of ACKR4 function in ceiling-LECs (cLECs) (12). However, our data have identified upstream DC migratory defects in *Ackr4*$^{-/-}$ mice. To determine the contribution of ACKR4 expressed in the skin on the arrival of DCs in the LN, we utilized a skin graft model (33) to restrict ACKR4 deficiency to cutaneous tissue. To validate the model, WT or *Ackr4*$^{-/-}$ skin was grafted onto WT hosts (*SI Appendix*, Fig. S4*A*), then CCL19 and CCL21 were measured in grafts and contralateral-flank host skin following a 6 wk recovery period to permit lymphatic repair (34). Both CCL19 and CCL21 were ~threefold higher in *Ackr4*$^{-/-}$ grafts compared to WT grafts, and no difference in chemokine abundance was observed in contralateral-flank host skin (*SI Appendix*, Fig. S4*B*). Next, WT and *Ackr4*$^{-/-}$ skin was grafted onto Ly5.1 hosts, and grafts were subsequently FITC-painted to permit enumeration of host-derived DCs emigrating from grafts to draining LNs (Fig. 3*H*). As anticipated, FITC^{+} DCs emigrating from WT grafts accumulated in graft-draining LNs and few FITC^{+} DCs cells were detected in the contralateral skin-draining LNs (Fig. 3*I*). Strikingly, there were significantly fewer FITC^{+} DCs in graft-draining LNs from *Ackr4*$^{-/-}$ graft recipients compared to WT controls, and there was no significant accumulation of FITC^{+} DCs in graft-draining LNs compared to contralateral LNs of *Ackr4*$^{-/-}$ graft recipients (Fig. 3*I*). Together, these data demonstrate that ACKR4-dependent regulation of dermal CCL21 is essential for efficient emigration of DCs to LNs. Thus, ACKR4 regulates DC migration from the skin to LNs independently of its function in the LN SCS (12).

ACKR4 Limits Pollution of Downstream LNs with Skin-Derived Soluble CCL21. Given the striking hyperabundance of soluble CCL21 in ear tissue of *Ackr4*$^{-/-}$ mice (Fig. 1) and the dysregulation of CCL21 seen in the LNs of *Ackr4*$^{-/-}$ mice (12, 23), we investigated whether excess soluble CCL21 in ACKR4-deficient skin drained via afferent lymphatics and polluted the LN reservoir of CCL21. Skin-draining LNs from *Ackr4*$^{-/-}$ mice contained a greater proportion of solubilized CCL21 than WT mice (Fig. 4 *A* and *B*). To determine the source of additional soluble CCL21 in ACKR4-deficient LNs, we took advantage of tissue-restricted murine *Ccl21* gene expression. In C57BL6/J mice, three genes encode two CCL21 isoforms that differ by one amino acid and are expressed in anatomically distinct compartments: *Ccl21a* encodes CCL21-serine-65 (CCL21-Ser) predominantly expressed in lymphoid tissues, and *Ccl21b*/*Ccl21c* encodes CCL21-leucine-65 (CCL21-Leu) expressed by LECs in peripheral tissues (31, 35, 36). Isolating soluble CCL21 from WT and *Ackr4*$^{-/-}$ LNs, the relative abundance of LN-produced CCL21-Ser and peripheral CCL21-Leu was determined by mass spectrometry (Fig. 4*C*). While this assay was technically challenging due to the hydrophobic nature of the only unique CCL21-Ser/Leu peptides, a consistently greater ratio of CCL21-Leu:CCL21-Ser was detected in LNs from *Ackr4*$^{-/-}$ mice (Fig. 4*D*), in keeping with increased leakage of soluble CCL21 from peripheral tissues. Previously, dysregulated LN CCL21 was attributed to loss of ACKR4 function in cLECs (12); however, the dysregulated dermal CCL21 identified here may contribute to that reported defect in *Ackr4*$^{-/-}$ mice. To determine the requirement of skin ACKR4 in regulating draining LN CCL21 abundance, CCL21 was measured in graft-draining and control contralateral LNs of skin-grafted mice (Fig. 3*H*). There was a greater abundance of CCL21 in the graft-draining LNs of *Ackr4*$^{-/-}$ graft recipients compared to control contralateral LNs and graft-draining LNs of WT graft recipients (Fig. 4*E*). These data demonstrate that skin ACKR4 is essential in regulating LN CCL21 abundance by restricting dissemination of CCL21 out of the skin. Despite cLEC ACKR4 function being intact in this model, it was not sufficient to limit LN pollution with peripheral CCL21, indicating it plays a supplementary role to ACKR4 in the skin with regard to regulation of CCL21 in LNs.

In conclusion, this study resolves long-standing differences in the reported contribution of ACKR4 in scavenging CCL21 in vivo. Reconciling these findings, we demonstrate that ACKR4 contributes to chemokine regulation in barrier tissues by scavenging soluble CCL21 to prevent dissemination from these tissues and shaping the immobilized CCL21 gradient to maintain it within an optimal range for efficient directional migration of DCs to LVs. Leveraging techniques to distinguish forms of CCL21, we demonstrate that cleaved CCL21 is generated at the steady state. This implies that soluble CCL21 is not just the product of mature DCs processing immobilized CCL21 but raises the possibility that semimature DCs migrating during the steady state similarly process CCL21. Additionally, given that immobilized, albeit hyperabundant, gradients were still observed in the absence of ACKR4-mediated scavenging, it is possible that basal cleavage of full-length CCL21 may function in tandem with diffusion to establish and maintain immobilized interstitial CCL21 gradients. To investigate the function of CCL21 cleavage in immobilized CCL21 gradient maintenance, models which lack CCL21 cleavage are required.

The biological role of soluble CCL21 in vivo is not understood. Indeed, studies with *St8sia4*$^{-/-}$ and *Grk6*$^{-/-}$ mice have demonstrated the dependence for DCs to sense full-length CCL21 for emigration from the skin. *St8sia4* is required for DCs to reconfigure full-length CCL21 from an autoinhibitory confirmation (37), while *Grk6* is required for CCR7 signal transduction following ligation with full-length CCL21 (30). Both *St8sia4* and *Grk6* are dispensable for CCR7 signaling following cleaved CCL21 ligation in vitro but are both essential for DC egress from skin (30, 37). Thus, cleaved CCL21 is thought to be redundant in DC egress from tissues. However, it is unknown whether de novo generation of soluble CCL21 by migrating DCs is sufficient to transiently guide or disrupt the migration of trailing DCs in vivo. Resolving these questions requires identification of the protease(s) involved in CCL21 processing and development of models that lack DC-mediated CCL21 processing capability. Interestingly, the serine protease plasmin has been demonstrated to cleave and solubilize CCL21 when bound to the surface of human DCs and T cells in vitro (38); however, it is unknown to what extent plasmin is captured by DCs and utilized for CCL21 cleavage in vivo. As plasmin mRNA was not detected in DCs (38), studies utilizing DCs deficient in plasminogen receptors are likely to be required to determine the contribution of DC-bound plasmin in CCL21 cleavage.

While an essential role for CCL19 has not been demonstrated in the steady-state egress of DCs in WT mice (16) or impaired DC egress in steady-state *Ackr4*$^{-/-}$ mice (19), aberrant DC egress in *Ackr4*$^{-/-}$ mice during cutaneous inflammation is rescued in *Ccl19*$^{-/-}$*Ackr4*$^{-/-}$ mice (19). Under inflammatory conditions, it is unclear how immobilized CCL21 and soluble CCL21 and CCL19 co-operate and interact to facilitate DC egress. Thus, future studies investigating the contributions of each of these functionally distinct CCR7 ligands should address how CCL21 cleavage, haptotactic migration, and CCL19 function together and regulate DC egress during inflammation.

Finally, in addition to these functions, ACKR4 in skin also limits dissemination of peripheral CCL21 to skin-draining LNs where CCL21 regulation was previously attributed to ACKR4 in LN cLECs (12). Therefore, the precise contribution of cLEC ACKR4 expression in LN CCL21 regulation will require development of models that restrict ACKR4 deletion to cLECs. Whether excess CCL21 also drains from LNs via the efferent lymphatics and pollutes the blood and other tissues remains unknown and requires models that restrict ACKR4 deletion to defined tissues. Given the findings that ACKR4 profoundly impacts T cell priming (12), autoimmune T cell responses (23), and antitumor immunity (24), a clear understanding of the mechanisms at play remain important issues.

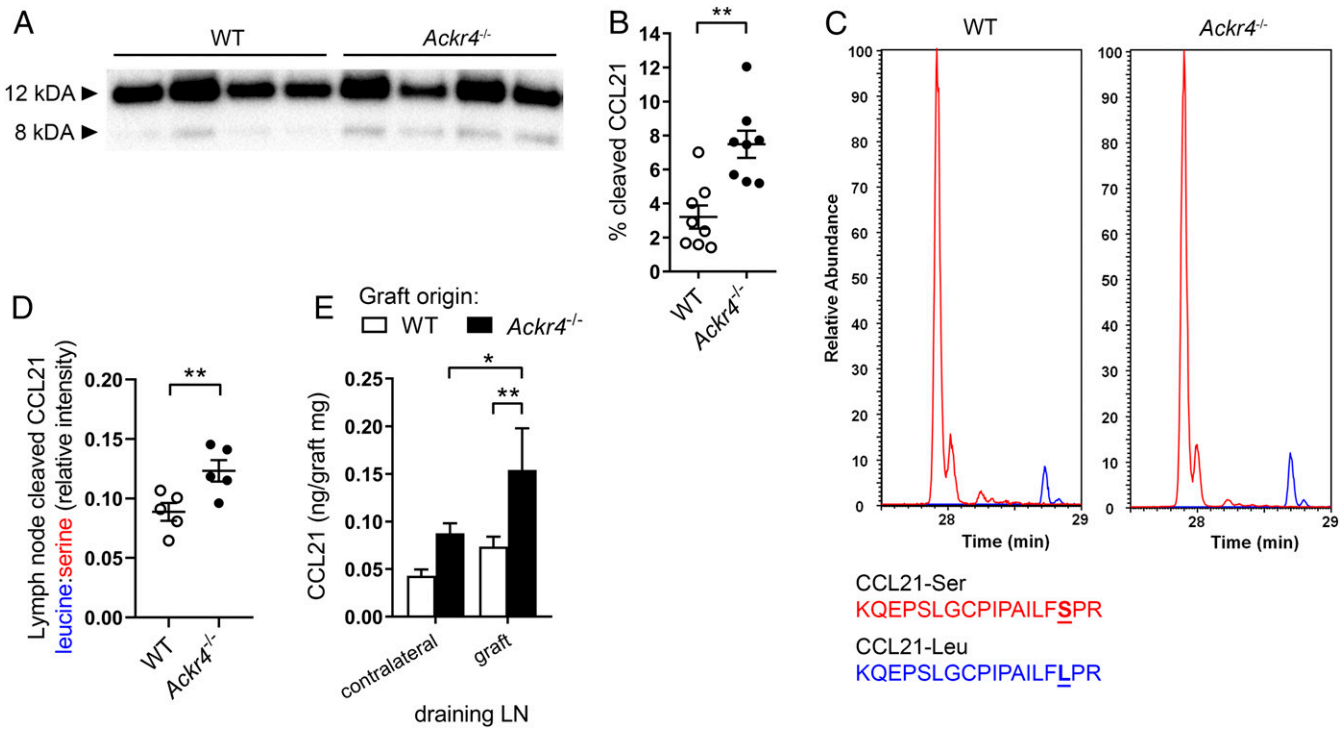

Fig. 4. Cutaneous ACKR4 restricts dissemination of peripheral CCL21 to draining LNs. (*A*) Detection of full-length and cleaved CCL21 leached out from skin-draining LNs (inguinal, axillary, and deep cervical) of resting WT and *Ackr4*$^{-/-}$ mice by immunoprecipitation, then Western blot. (*B*) Percent cleaved CCL21 of total CCL21 in skin-draining LNs from *A*. (*C*) Representative LC–MS chromatograms detecting unique CCL21-Ser (red) and CCL21-Leu (blue) tryptic peptides from cleaved CCL21 leached out and immunoprecipitated from skin-draining LNs of steady-state WT and *Ackr4*$^{-/-}$ mice. Unique CCL21-Ser and CCL21-Leu tryptic peptide sequences with single amino acid difference underlined. (*D*) Relative intensity of CCL21 leucine:serine isoforms quantitated from LC–MS analysis. (*E*) Quantity of total CCL21 (nanogram/graft milligram) in graft draining and contralateral LNs in skin-grafted mice from Fig. 3*H*. Data are relative to graft weight (milligram). (*A*) Blots representative of two independent experiments, $n = 8$ biological samples of two pooled mice per genotype, each lane is a biological sample. (*B*) Pooled from two independent experiments, $n = 8$ biological samples of two pooled mice per genotype. Each dot is one biological sample, ± SEM, two-tailed unpaired Student's *t* test. (*C* and *D*) Representative of two independent experiments, (*C*) LC–MS quantitation of CCL21 leucine:serine, mean ± SEM ($n = 5$ biological samples of two pooled mice per genotype), two-tailed unpaired Student's *t* test. (*E*) Pooled from three independent experiments, $n = 14$ WT graft recipients, $n = 5$ *Ackr4*$^{-/-}$ graft recipients, ± SEM, two-way ANOVA with Sidak's multiple comparison test. $^{*}P < 0.05$ and $^{**}P < 0.01$.

Materials and Methods

Mice and Bone Marrow Reconstitutions. C57BL/6J and Ly5.1 (B6.SJL.*Ptprca*) mice were purchased from the Animal Resource Centre or bred and maintained at Laboratory Animal Services, University of Adelaide. *Ackr4*$^{-/-}$ and Ly5.1 *Ackr4*$^{-/-}$ mice were bred and maintained at Laboratory Animal Services, University of Adelaide. Tissues from 129SV mice were obtained from the Core Animal Facility, University of South Australia Cancer Research Institute. Bone marrow chimeric mice were generated by reconstituting lethally irradiated mice (1,000 Rads) with 5×10^6 total bone marrow cells from strains indicated in the text. Chimeric mice were rested for 8 wk prior to use. All experiments were approved by the University of Adelaide Animal Ethics Committee.

Flow Cytometry and Cell Sorting. To prepare skin-cell suspensions, ears were dissected, split, and floated on 20 mM EDTA/phosphate-buffered saline (PBS) for 2 h at 37 °C. Dermal and epidermal sheets were separated and then minced and incubated in digestion buffer (Dulbecco's modified Eagle medium with 5% FCS, 2.5 mM $CaCl_2$, 10 mM HEPES and 0.2 U/mL penicillin/streptomycin) supplemented with 85 μg/mL Liberase TM (Roche) and 30 U/mL DNase-I (Sigma) at 37 °C for 1.5 h with occasional mixing. LNs were harvested into digestion buffer with 1 mg/mL collagenase (Sigma-Aldrich), gently minced, and incubated for 30 min at 37 °C. Cell suspensions were passed through 70 μm cell strainers (BD Biosciences), counted, and stained with antibody mixtures in PBS/1% BSA/0.04% sodium azide. Fc-receptors were blocked with mouse γ-globulin (Rockland), and dead cells were excluded from all analyses with LIVE/DEAD dye (Molecular Probes, L10119). The following antibodies and secondaries were used: anti-CD45 (553081); anti-EpCAM (552370); mouse-Ter119 (561071); anti-CD31 (553372); anti–CD140α (562774); anti-CD90.2 (553007); anti–IA-IE (553622); anti-B220 (562922); anti-CD45.1 (560580); anti-CD11c (563735); anti-I-A^b (562823); streptavidin PerCPCy5.5 (551419) from BD Biosciences; anti-gp38 (13-5381) from eBioscience; anti-CD45.2 (109830) and anti-CD11c (117327) from BioLegend; and anti-rat IgG-AF647 (Molecular Probes, A21247). Flow cytometry and cell sorting were performed on a FACSAria (BD Biosciences) with a 100 μm nozzle at 20 psi, and data were analyzed with FlowJo software (BD Biosciences).

Extraction of Tissue Chemokines. Tissues were harvested after cardiac perfusion, weighed, and incubated in PBS containing protease inhibitor and PMSF (Sigma) with shaking for 3 h at 4 °C. Supernatants were isolated following centrifugation and stored at −80 °C until use.

Chemokine Quantification by ELISA. ELISA was performed on supernatants as previously described (23) with anti-CCL19 (MAB880), biotinylated anti-CCL19 (BAF880), polyclonal goat anti-CCL21 (AF457) for total CCL21, monoclonal rat anti-CCL21 (MAB457) for full-length CCL21, biotinylated anti-CCL21 (BAF457), anti-CCL25 (MAB4811), biotinylated anti-CCL25 (BAF481) from R&D Systems, and streptavidin-HRP (Rockland). Reactions were developed with TMB substrate (eBioscience), stopped with 1 M orthophosphoric acid, and analyzed at 450 nm (Amersham Biosciences Biotrak II plate reader). Concentrations of chemokines were calculated from standard curves generated with GraphPad Prism.

Generation of Cleaved CCL21. Cleaved CCL21 was generated by incubating 200 ng of recombinant mouse CCL21 (R&D Systems) with 6×10^5 BMDCs for 12 h at 37 °C, 5% CO_2. Culture supernatants containing CCL21 were directly separated by gel electrophoresis without immunoprecipitation.

Immunoprecipitation of Endogenous CCL21. Tissue supernatants were prepared as above from inguinal, axillary, and deep cervical LNs. CCL21 was immunoprecipitated

from supernatants with Protein G Dynabeads (Invitrogen) washed in 0.02% Tween20 and loaded with polyclonal goat anti-CCL21 (R&D Systems; AF457). LN CCL21 was pooled from two mice by sequentially immunoprecipitating individual supernatants, then samples were extensively washed.

Protein Gel Electrophoresis and Western Blots. Samples were resuspended in 2× Laemmli sample buffer (Bio-Rad) with 1 M DTT, then separated by sodium dodecyl sulfate–polyacrylamide gel electrophoresis on 4 to 12% Bolt gels (Invitrogen) in MES Buffer (Invitrogen). Full-length and cleaved CCL21 were identified by molecular ladders and controls. For mass spectrometry analysis, gel bands were visualized with Oriole stain (Bio-Rad), excised, then stored at 4 °C in Eppendorf tubes until processed. For Western blot analyses, gels were semidry transferred to 0.2 μm PVDF membranes in discontinuous Tris-CAPS buffer, then blocked with 3% BSA Tris 0.1% Tween20. Membranes were incubated with biotinylated polyclonal goat anti-CCL21 (R&D Systems; AF457) or monoclonal rat anti-CCL21 (R&D Systems; MAB457), washed in 3% BSA Tris 0.1% Tween20, incubated with streptavidin-HRP or HRP-conjugated anti-rat IgG (Jackson ImmunoResearch, 712-036-150), then washed and developed with Immobilon Crescendo Western HRP substrate (Millipore). Some membranes were reprobed with polyclonal rabbit anti-CCL21 (Peprotech, 500-P114) and HRP-conjugated anti-rabbit IgG (Invitrogen, 31460). Blots were imaged on a Bio-Rad ChemiDoc MP with Image Lab 6.0 software. Percentage of cleaved CCL21 was calculated with the Volume tool in Image Lab 6.0.

Mass Spectrometry. Gel bands containing CCL21 isoforms were processed by in-gel digestion as previously described (39), with the resulting tryptic peptides desalted by ZipTips (Merck Millipore). Liquid chromatography–mass spectrometry (LC–MS) analysis was performed on an Ultimate 3000 RSLCnano system coupled to an Orbitrap Exploris 480 mass spectrometer (Thermo Scientific). Samples were resuspended in 20% acetonitrile and 0.1% formic acid before injection onto a 25 cm fused silica analytical column (75 μm internal diameter packed in-house with 1.9 μm C18 particles) heated at 50 °C. Peptide elution was performed at a 300 nL/min flow rate using a 10 min linear gradient (20 to 56% acetonitrile in 0.1% formic acid). A targeted tandem mass spectrometry method (40) was employed to detect the triply charged carboxyamidomethylated peptides of CCL21A (KQEPSLGCPIPAILFSPR) and CCL21B (KQEPSLGCPIPAILFLPR), with their respective abundances represented by the intensities of PIPAILFSPR (*m/z* 900.53016) and PIPAILFLPR (*m/z* 926.58220) fragment ions acquired at resolution 30,000 (*m/z* 200).

qPCR Analysis. Large, snap-frozen tissue samples were homogenized with a mortar and pestle under liquid nitrogen, decanted, and mixed with 1 mL TRIzol (Ambion) per 100 mg starting tissue. RNA was extracted according to manufacturer's protocol. RNA was extracted from sorted cells using either the QIAGEN RNeasy Micro Kit or QIAGEN RNeasy Mini Kit according to manufacturer's protocol, including on-column DNase digest. Complementary DNA (cDNA) was synthesized from isolated RNA with the Transcriptor First Strand cDNA Synthesis Kit (Roche) according to manufacturer's protocol. qPCR was performed with SYBR Green I Master Kit (Roche) on a LightCycler 480 (Roche) according to manufacturer's protocol, and data were analyzed with LightCycler 480 SW 1.5 software (Roche). Primers were designed with Primer Express 3.0 software (Thermo Fisher Scientific), and specificity was confirmed using the National Center for Biotechnology Information Primer-BLAST tool prior to synthesis (Sigma-Aldrich). Relative expression was calculated with the $1/2^{\Delta CT}$ method, where $\Delta CT = Ct_{Target} - Ct_{RPLP0}$. The following primers were used: *Rplp0* forward 5′-AGATGCAGCAGATCCGCAT-3′, reverse 5′-GGATGGCCTTGCGCA-3′; *Ackr4* forward 5′-AATGCTAGGTGCACT-CCCATCT-3′, reverse 5′-CCGATTTCCAGCATCTGAATG-3′; *Ccl21* forward 5′-GCA-AAGAGGGAGCTAGAAAACAGA-3′, reverse 5′-TGGACGGAGGCCAGCAT-3′, *Ccl19* forward 5′-CCTGGGTGGATCGCATCA-3′, reverse 5′-TGCCTTTGTTCTTGGCAGAA-3′; and *Ccl25* forward 5′-GACTGCTGCCTGGGTTACCA-3′, reverse 5′-CCTAGCATG-CCGGAGAACA-3′.

Whole-Mount Immunofluorescence. Mouse ears were mechanically split, limiting cartilage and fat on ventral sheets. Immobilized CCL21 gradients were stained as described elsewhere (8). The following antibodies and secondaries were used: anti-LYVE-1 (R&D Systems, MAB2125), anti-CCL21 (R&D Systems, BAF457), anti-CD31 (BD Biosciences, 550274), anti-rat IgG-AF488 (Molecular Probes, A11006), anti-rat IgG-FITC (Jackson, 712-095-153), and streptavidin-AF647 (Jackson, 016-600-084). Ear tissue was mounted on polysine slides (Thermo Scientific) with Vectorshield (Vector).

BMDC Ear Crawl In. BMDCs were generated, and crawl-in assays were performed as described elsewhere (41) with minor modifications. Briefly, BMDCs were labeled with Cell Proliferation Dye eFluor670 (eBioscience) and incubated for 45 min at 37 °C, 5% CO_2 atop ventral ear tissue mounted with a 6 × 12 × 1.2 mm metal washer sealed with 2% agarose. Migratory apparatus were dismantled, and ear sections were washed in PBS, fixed in 1% PFA, and mounted on polysine slides (Thermo Scientific) with Vectorshield (Vector).

Confocal Microscopy and Image Analysis. Z-stack images were acquired on a Leica TCS SP5 confocal microscope at room temperature with a 10× harmonically corrected plan apochromat with NA 0.4, or 20× harmonically corrected plan apochromat with NA 0.7 water objective, using Leica Application Suite: Advance Fluorescence software and sequential scanning between frames. Max-projections and all data analyses were performed in FIJI (ImageJ, NIH). To quantitate BMDC accumulation in LVs after crawl-in assays, LV areas were defined from max-projected LYVE-1 single-channel images. The Cell Tracker mean gray intensity of labeled BMDCs was subsequently measured from max-projected BMDC single channels within LYVE-1$^+$ and LYVE-1$^-$ areas. Data are presented as the ratio of Cell Tracker mean gray intensity inside:outside LYVE-1$^+$ areas. To measure CCL21 intensity at defined distances from LVs, Z-stack images of 15 to 32 μm at 1 μm intervals encompassing LV were used. First, distance maps were created from max-projected LYVE-1 single-channel images with FIJI. From these distance maps, consecutive 10 pixel (7.6 μm) wide regions surrounding the vessels were defined, starting at the LV edge then extending incrementally ∼90 μm into the interstitial space. The CCL21 mean gray intensity was subsequently measured within each of these regions from the max-projected CCL21 single-channel image. Measured CCL21 mean gray values were then normalized to the average CCL21 intensity across all WT images within the independent experiment. The image scale was subsequently applied to convert the pixel distance of each region from vessels to μm, and distances were plotted on graphs as the minimum distance of the range each region was located from the nearest LV. The same process was followed for CD31$^+$ vessels. Brightness and contrast adjustments were applied equally across images with Adobe Photoshop CS6.

Intravital Imaging and BMDC Tracking. Intravital imaging of the footpad was performed using a modified version of a published protocol (9). Briefly, activated BMDCs were harvested, labeled with CellTrace Violet (Molecular Probes), and 1 to 2 × 10^6 labeled BMDCs mixed with 50 ng LPS in a final volume of 60 μL were injected subcutaneously into the footpad of anesthetized WT or *Ackr4*$^{-/-}$ recipient mice. To label LVs, 5 μg anti–LYVE-1-AF594 (R&D Systems, conjugated in-house with AF594 Monoclonal Antibody Labeling Kit, Invitrogen) was coinjected subcutaneously into the footpad. Imaging of the footpad was performed between 12 to 21 h postinjection. For visualization of blood vasculature, 50 μL of 0.1% Evans Blue (Sigma) dissolved in PBS was administered intravenously. Time-lapse imaging was performed using an upright FVMPE-RS multiphoton microscope (Olympus) equipped with at 25×/1.0 NA water-immersion lens, enclosed in a custom-built environmental chamber (Precision Plastics) that was maintained at 35 °C with heated air while mice were maintained on a heat pad at 37 °C. Fluorescence excitations were performed at 800 nm using an InSight pulsed infrared laser (Spectra Physics). Image stacks were acquired every minute over an hour imaging period. Imaging data were processed in Imaris 8.1.2 (Bitplane). Images were corrected for drift using static blood vasculature, then LVs were rendered in three dimensions, and a distance transformation on the outside surface of the vessels was performed using a Matlab extension. BMDCs that could be clearly followed were manually tracked and the mean speed, track straightness, length, and duration were calculated using statistics tools in Imaris. BMDC distance from the nearest lymphatic vessel was determined with the generated distance transformation channel across all time points tracked. The following parameters were then calculated: BMDC velocity toward LVs = displacement relative to nearest LV (micrometers)/track duration (minutes), and lymphatic vessel homing efficiency = displacement relative to nearest LV (micrometers)/track length (micrometers).

Skin Grafting and FITC Paint. Skin grafting was performed as previously described (42) with minor modifications. Briefly, anesthetized host mice were shaved between the front and back legs on their right flank with electric clippers. Incisions in the flank skin down to the panniculus carnosus were cut to fit two ear sheets separated by ∼2 mm of skin, then the tissue was removed. Graft tissue was laid on resulting graft beds and trimmed accordingly. Mice were bandaged and received subcutaneous analgesic. Bandages were removed after 7 d, and mice were rested for a further 5 wk before experimentation. For FITC painting experiments, a 10% solution of FITC (Sigma-Aldrich) in dimethyl sulfoxide was prepared, then diluted to 1% FITC in a 1:1 mix of acetone:dibutyl phthalate. Mice were anesthetized via isoflurane inhalation, and 10 μL of 1% FITC was slowly pipetted onto grafts. After 48 h, inguinal, axillary, and brachial LNs were harvested for DC and CCL21 quantitation. Measures are relative to graft weight (milligrams) to account for any intermouse variation in graft size.

Mice where FITC application was not confined to grafted tissue were excluded from DC analyses.

Statistical Analyses. All statistical analyses were performed in GraphPad Prism with the statistical tests described in the text. A $P < 0.05$ was considered significant.

Data Availability. All study data are included in the article and/or supporting information.

ACKNOWLEDGMENTS. We thank Dr. Josef Nguyen (Royal Adelaide Hospital, Adelaide, Australia) for mouse irradiation; the staff of Laboratory Animal Services, University of Adelaide, for animal husbandry; Dr. Denise Noonan for veterinary assistance; and Dr. Agatha Labrinidis and Lynette Waterhouse (Adelaide Microscopy, University of Adelaide) for imaging assistance. P.H., C.Y., and M.R.C. acknowledge Bioplatforms Australia, the University of South Australia, and the state and federal governments, which cofund the National Collaborative Research Infrastructure Strategy-enabled Mass Spectrometry and Proteomics facility at the University of South Australia. C.R.B. was supported by an Australian Postgraduate Award.

1. T. Worbs *et al*., Oral tolerance originates in the intestinal immune system and relies on antigen carriage by dendritic cells. *J. Exp. Med.* **203**, 519–527 (2006).
2. R. Förster *et al*., CCR7 coordinates the primary immune response by establishing functional microenvironments in secondary lymphoid organs. *Cell* **99**, 23–33 (1999).
3. A. Martln-Fontecha *et al*., Regulation of dendritic cell migration to the draining lymph node: Impact on T lymphocyte traffic and priming. *J. Exp. Med.* **198**, 615–621 (2003).
4. L. Ohl *et al*., CCR7 governs skin dendritic cell migration under inflammatory and steady-state conditions. *Immunity* **21**, 279–288 (2004).
5. G. Hintzen *et al*., Induction of tolerance to innocuous inhaled antigen relies on a CCR7-dependent dendritic cell-mediated antigen transport to the bronchial lymph node. *J. Immunol.* **177**, 7346–7354 (2006).
6. E. Kriehuber *et al*., Isolation and characterization of dermal lymphatic and blood endothelial cells reveal stable and functionally specialized cell lineages. *J. Exp. Med.* **194**, 797–808 (2001).
7. M. D. Gunn *et al*., A chemokine expressed in lymphoid high endothelial venules promotes the adhesion and chemotaxis of naive T lymphocytes. *Proc. Natl. Acad. Sci. U.S.A.* **95**, 258–263 (1998).
8. M. Weber *et al*., Interstitial dendritic cell guidance by haptotactic chemokine gradients. *Science* **339**, 328–332 (2013).
9. O. Tal *et al*., DC mobilization from the skin requires docking to immobilized CCL21 on lymphatic endothelium and intralymphatic crawling. *J. Exp. Med.* **208**, 2141–2153 (2011).
10. K. Vaahtomeri *et al*., Locally triggered release of the chemokine CCL21 promotes dendritic cell transmigration across lymphatic endothelia. *Cell Rep.* **19**, 902–909 (2017).
11. E. Russo *et al*., Intralymphatic CCL21 promotes tissue egress of dendritic cells through afferent lymphatic vessels. *Cell Rep.* **14**, 1723–1734 (2016).
12. M. H. Ulvmar *et al*., The atypical chemokine receptor CCRL1 shapes functional CCL21 gradients in lymph nodes. *Nat. Immunol.* **15**, 623–630 (2014).
13. K. Schumann *et al*., Immobilized chemokine fields and soluble chemokine gradients cooperatively shape migration patterns of dendritic cells. *Immunity* **32**, 703–713 (2010).
14. G. M. Hjortø *et al*., Differential CCR7 targeting in dendritic cells by three naturally occurring CC-chemokines. *Front. Immunol.* **7**, 568 (2016).
15. M. A. Hauser, D. F. Legler, Common and biased signaling pathways of the chemokine receptor CCR7 elicited by its ligands CCL19 and CCL21 in leukocytes. *J. Leukoc. Biol.* **99**, 869–882 (2016).
16. M. R. Britschgi, S. Favre, S. A. Luther, CCL21 is sufficient to mediate DC migration, maturation and function in the absence of CCL19. *Eur. J. Immunol.* **40**, 1266–1271 (2010).
17. N. A. Moussouras *et al*., Structural features of an extended C-terminal tail modulate the function of the chemokine CCL21. *Biochemistry* **59**, 1338–1350 (2020).
18. K. Heinzel, C. Benz, C. C. Bleul, A silent chemokine receptor regulates steady-state leukocyte homing in vivo. *Proc. Natl. Acad. Sci. U.S.A.* **104**, 8421–8426 (2007).
19. S. A. Bryce *et al*., ACKR4 on stromal cells scavenges CCL19 to enable CCR7-dependent trafficking of APCs from inflamed skin to lymph nodes. *J. Immunol.* **196**, 3341–3353 (2016).
20. C. A. Thomson *et al*., Expression of the atypical chemokine receptor ACKR4 identifies a novel population of intestinal submucosal fibroblasts that preferentially expresses endothelial cell regulators. *J. Immunol.* **201**, 215–229 (2018).
21. B. Lucas *et al*., CCRL1/ACKR4 is expressed in key thymic microenvironments but is dispensable for T lymphopoiesis at steady state in adult mice. *Eur. J. Immunol.* **45**, 574–583 (2015).
22. E. E. Kara *et al*., Atypical chemokine receptor 4 shapes activated B cell fate. *J. Exp. Med.* **215**, 801–813 (2018).
23. I. Comerford *et al*., The atypical chemokine receptor CCX-CKR scavenges homeostatic chemokines in circulation and tissues and suppresses Th17 responses. *Blood* **116**, 4130–4140 (2010).
24. C. E. Whyte *et al*., ACKR4 restrains antitumor immunity by regulating CCL21. *J. Exp. Med.* **217**, e20190634 (2020).
25. M. D. Bunting *et al*., CCX-CKR deficiency alters thymic stroma impairing thymocyte development and promoting autoimmunity. *Blood* **121**, 118–128 (2013).
26. N. Eckert, K. Werth, S. Willenzon, L. Tan, R. Förster, B cell hyperactivation in an Ackr4-deficient mouse strain is not caused by lack of ACKR4 expression. *J. Leukoc. Biol.* **107**, 1155–1166 (2020).
27. M. Merad *et al*., Langerhans cells renew in the skin throughout life under steady-state conditions. *Nat. Immunol.* **3**, 1135–1141 (2002).
28. D. G. Janson, G. Saintigny, A. van Adrichem, C. Mahé, A. El Ghalbzouri, Different gene expression patterns in human papillary and reticular fibroblasts. *J. Invest. Dermatol.* **132**, 2565–2572 (2012).
29. T. Krausgruber *et al*., Structural cells are key regulators of organ-specific immune responses. *Nature* **583**, 296–302 (2020).
30. J. Schwarz *et al*., Dendritic cells interpret haptotactic chemokine gradients in a manner governed by signal-to-noise ratio and dependent on GRK6. *Curr. Biol.* **27**, 1314–1325 (2017).
31. S. C. Chen *et al*., Ectopic expression of the murine chemokines CCL21a and CCL21b induces the formation of lymph node-like structures in pancreas, but not skin, of transgenic mice. *J. Immunol.* **168**, 1001–1008 (2002).
32. P. Vargas *et al*., Innate control of actin nucleation determines two distinct migration behaviours in dendritic cells. *Nat. Cell Biol.* **18**, 43–53 (2016).
33. L. A. Dunn *et al*., Presentation of the HPV16E7 protein by skin grafts is insufficient to allow graft rejection in an E7-primed animal. *Virology* **235**, 94–103 (1997).
34. A. Yan, T. Avraham, J. C. Zampell, S. Z. Aschen, B. J. Mehrara, Mechanisms of lymphatic regeneration after tissue transfer. *PLoS One* **6**, e17201 (2011).
35. G. Vassileva *et al*., The reduced expression of 6Ckine in the plt mouse results from the deletion of one of two 6Ckine genes. *J. Exp. Med.* **190**, 1183–1188 (1999).
36. H. Nakano, M. D. Gunn, Gene duplications at the chemokine locus on mouse chromosome 4: Multiple strain-specific haplotypes and the deletion of secondary lymphoid-organ chemokine and EBI-1 ligand chemokine genes in the plt mutation. *J. Immunol.* **166**, 361–369 (2001).
37. E. Kiermaier *et al*., Polysialylation controls dendritic cell trafficking by regulating chemokine recognition. *Science* **351**, 186–190 (2016).
38. N. Lorenz *et al*., Plasmin and regulators of plasmin activity control the migratory capacity and adhesion of human T cells and dendritic cells by regulating cleavage of the chemokine CCL21. *Immunol. Cell Biol.* **94**, 955–963 (2016).
39. A. Shevchenko, H. Tomas, J. Havlis, J. V. Olsen, M. Mann, In-gel digestion for mass spectrometric characterization of proteins and proteomes. *Nat. Protoc.* **1**, 2856–2860 (2006).
40. A. C. Peterson, J. D. Russell, D. J. Bailey, M. S. Westphall, J. J. Coon, Parallel reaction monitoring for high resolution and high mass accuracy quantitative, targeted proteomics. *Mol. Cell. Proteomics* **11**, 1475–1488 (2012).
41. M. Weber, M. Sixt, Live cell imaging of chemotactic dendritic cell migration in explanted mouse ear preparations. *Methods Mol. Biol.* **1013**, 215–226 (2013).
42. I. H. Frazer *et al*., Tolerance or immunity to a tumor antigen expressed in somatic cells can be determined by systemic proinflammatory signals at the time of first antigen exposure. *J. Immunol.* **167**, 6180–6187 (2001).